

Spatial regularity of the young stellar population in spiral arms of late type galaxies NGC 895, NGC 5474, and NGC 6946

A. S. Gusev,[★] E. V. Shimanovskaya and N. A. Zaitseva

Sternberg Astronomical Institute, Lomonosov Moscow State University, Universitetsky pr. 13, 119234 Moscow, Russia

Accepted 2022 June 6. Received 2022 June 3; in original form 2022 April 20

ABSTRACT

We investigate the spatial regularity in the distribution of the young stellar population along spiral arms of three late type spiral galaxies: NGC 895, NGC 5474, and NGC 6946. This study is based on an analysis of photometric properties of spiral arms using *GALEX* ultraviolet, optical *UBVRI*, $H\alpha$, and $8\mu\text{m}$ *IRAC* infrared surface photometry data. Using the Fourier analysis approach, we found features of spatial regularity or quasi-regularity in the distribution of the young stellar population or (and) regular chains of star formation regions in all arms of NGC 895, NGC 5474, and NGC 6946 with characteristic scales of spacing from 350 to 500 pc in different arms, and (or) scales which are multiples of them. These characteristic scales are close to the those found earlier in NGC 628, NGC 6217, and M100.

Key words: galaxies: individual: NGC 895, NGC 5474, NGC 6946 – H II regions – open clusters and associations: general – galaxies: ISM – galaxies: spiral

1 INTRODUCTION

Young stars are usually associated with spiral arms of disc galaxies. They are concentrated along the spiral arms non-uniformly and form hierarchical groupings of different scales (see, e.g., Efremov & Elmegreen 1998). Sites of star formation are connected by unity of an origin with their ancestors – the molecular clouds. Gravitational collapse and turbulence compression are suspected to play a key role in the creation and evolution of star formation regions. Spatial distribution of star formation regions in discs of spiral galaxies can be explained in terms of gravitational or magnetogravitational instability (see, e.g., Elmegreen 1994, 2009, and references therein).

The regular spatial distribution of young stellar population in spiral arms is a rather rare phenomenon (Elmegreen & Elmegreen 1983). Actually, theoretical studies of the gravitational instability of a gaseous (Safronov 1960; Elmegreen & Elmegreen 1983), stellar-gaseous (Jog & Solomon 1984a,b; Romeo & Falstad 2013), and multicomponent disc (Rafikov 2001) predict regularity in the distribution of molecular clouds and star formation regions at constant gas, Σ_g , and stellar, Σ_s , surface densities, gas sound speed, c_g , and stellar velocity dispersion, σ_s , on sufficiently large scales within a galactic disc.

The results of the study of the fragmentation of gas filaments (Inutsuka & Miyama 1997; Mattern et al. 2018) and multicomponent spiral arms (Inoue & Yoshida 2018) also show the need for the constancy of the parameters of the stellar and interstellar medium

along the filaments (spiral arms) for the formation of spatial regularities in distribution of star formation regions.

Note that theoretical calculations of the disc instability, as well as calculations of fragmentation of spiral arms, predict regularities on scales of a few kpc for typical values of parameters of the stellar and interstellar medium (Elmegreen & Elmegreen 1983; Marchuk 2018; Inoue et al. 2021).

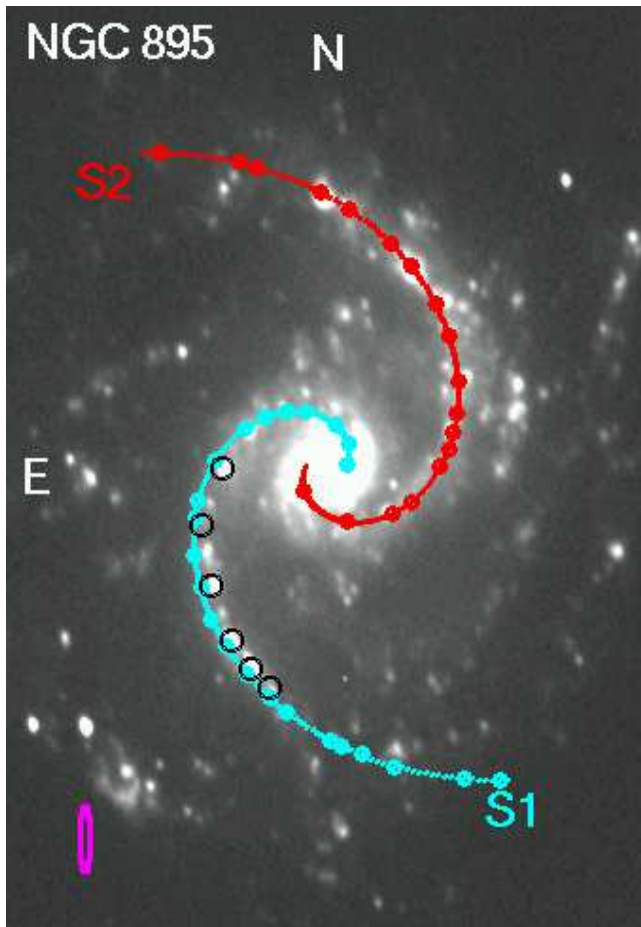
The first studies on finding regularities seemed to confirm the theoretical models. Elmegreen & Elmegreen (1983) found the regular strings of star complexes (H II regions) in spiral arms of 22 grand design galaxies with a characteristic spacing within 1–4 kpc. Efremov (2009, 2010) found the regularities in the distribution of H I superclouds in spiral arms of our Galaxy and in the distribution of star complexes in M31. He estimated the average spacing between the H I superclouds in the Carina spiral arm to be 1.5 kpc and in the Cygnus arm to be 1.3 kpc. He also found a regular string of star complexes in the north-western arm of M31 with a spacing of 1.1 kpc using *GALEX* UV images.

However, later there were indications of the presence of spatial regularities on sub-kpc scales. Gusev & Efremov (2013) noted the existence of the same characteristic separation (≈ 400 pc) between adjacent star formation regions in both spiral arms of NGC 628. Elmegreen, Elmegreen & Efremov (2018) found regularly spaced infrared peaks in the dusty spiral arms of M100 with a typical separation between them of ≈ 410 pc. Finally, Gusev & Shimanovskaya (2020) estimated a regular characteristic spacing to be ≈ 670 pc between adjacent young stellar groupings in the ring of NGC 6217 with the suspicion an existence of characteristic separation with a half scale along the ring. Proshina, Moiseev & Sil'chenko (2022)

[★] E-mail: gusev@sai.msu.ru

Table 1. The galaxy sample.

Galaxy	Type	B_t (mag)	M_B^a (mag)	Inclination (degree)	PA (degree)	R_{25}^c (arcmin)	R_{25}^c (kpc)	d (Mpc)	$A(B)_{\text{Gal}}$ (mag)	$A(B)_{\text{in}}$ (mag)
1	2	3	4	5	6	7	8	9	10	11
NGC 895	SA(s)cd	12.30	-20.84	49	105	1.70	16.1	32.7	0.092	0.31
NGC 5474	SA(s)cd pec	11.48	-18.07	50	100	1.20	2.3	6.7	0.038	0.33
NGC 6946	SAB(rs)cd	9.75	-20.68	31	62	7.74	13.3	5.9	1.241	0.04

^a Absolute magnitude of a galaxy corrected for Galactic extinction and inclination effects.^b Heliocentric radial velocity.^c Radius of a galaxy at the isophotal level 25 mag arcsec⁻² in the B band corrected for Galactic extinction and inclination effects.**Figure 1.** Deprojected image of NGC 895 in the $H\alpha$ line with overlaid logarithmic spirals S1 (cyan) and S2 (red). The cyan and red circles on the curves of the arms correspond to the positions of the local maxima of brightness. Positions of star formation complexes ($H\text{II}$ regions) from the list of Elmegreen & Elmegreen (1983) are indicated by open black circles. Example of used elliptical aperture ($18 \times 3 \text{ arcsec}^2$) is shown in magenta. North is upward and east is to the left.

found a similar regular separation, $\sim 700 \text{ pc}$, for star formation regions in the ring of the lenticular galaxy NGC 4324.

The aim of this study is to further search for spatial regularities in the distribution of young stellar population in the spiral arms of galaxies and to estimate their characteristic spacing. We also want

to understand how typical the spacing of $\sim 0.5 \text{ kpc}$ found earlier in NGC 628 and M100?

For this study we selected three late type spiral galaxies: NGC 895, NGC 5474, and NGC 6946 (Table 1). Despite the similar morphological type, Scd, these galaxies have different structural features. NGC 895 is a classic grand design two-arms spiral (Fig. 1). NGC 5474 is an asymmetric spiral galaxy with three arms located on one side of the centre (Fig. 2). Well known NGC 6946 is seen as a rather flocculent (Fig. 3), however it has a regular spiral density wave (Kendall, Kennicutt & Clarke 2011; Ghosh & Jog 2016). Two of the three galaxies, NGC 895 and NGC 5474, are on the list of Elmegreen & Elmegreen (1983).

NGC 5474 is about 10 times less massive and fainter than two other targets (see Table 1). It is similar to LMC in terms of mass and luminosity. The $H\text{I}$ mass in NGC 5474 is also approximately 10 times less than that in NGC 6946 (Rownd, Dickey & Helou 1994; Walter et al. 2008), however, H_2 -to- $H\text{I}$ mass ratio is equal to 0.86 in NGC 6946 (Leroy et al. 2009), but it does not reach 0.06 in NGC 5474 (Wilson et al. 2012).

We use *GALEX* ultraviolet *FUV* and *NUV*, optical *UBVRI* and $H\alpha$ surface photometry data for the analysis of the spatial distribution of the young stellar population along the spiral arms of galaxies. Additionally, we use the available *IRAC* $8 \mu\text{m}$ data for the NGC 6946.

The fundamental parameters of the galaxies are presented in Table 1, where the morphological type, Galactic absorption, $A(B)_{\text{Gal}}$, and the distance are taken from the NED¹ database, and the remaining parameters are taken from the LEDA² data base. The adopted value of the Hubble constant is equal to $H_0 = 75 \text{ km s}^{-1} \text{ Mpc}^{-1}$. With the assumed distances to the galaxies, we estimate their linear scales of 159, 32.5, and $28.6 \text{ pc arcsec}^{-1}$ for NGC 895, NGC 5474, and NGC 6946, respectively.

2 OBSERVATIONS AND DATA REDUCTION

2.1 Observational data

Our own photometric *UBVRI* and $H\alpha + [\text{NII}]$ observations of NGC 6946 and data reduction were described earlier in Gusev et al. (2016).

Images of NGC 895 and NGC 5474 in $H\alpha$ line were downloaded via NED database. The image of NGC 895 was obtained in the *Survey for Ionization in Neutral Gas Galaxies (SINGG)*³

¹ <http://ned.ipac.caltech.edu/>² <http://leda.univ-lyon1.fr/>³ <http://sungg.pha.jhu.edu/>

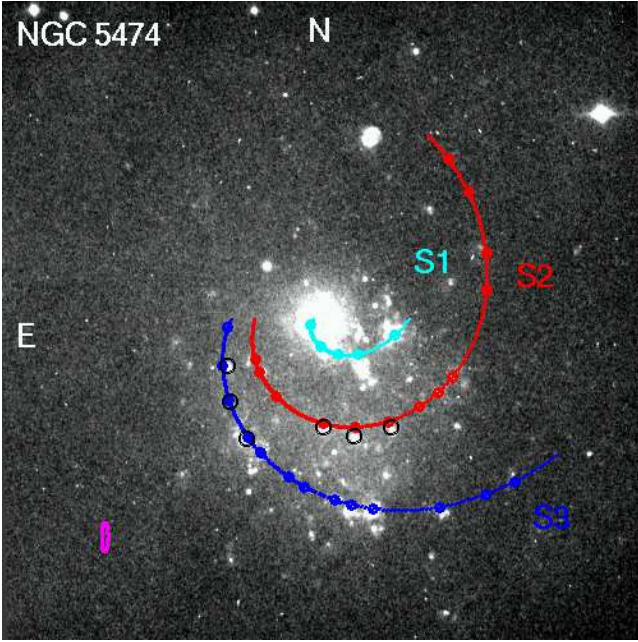


Figure 2. The same as Fig. 1, but for NGC 5474. Logarithmic spiral S3 is shown in blue. The size of the used elliptical aperture is $18 \times 4 \text{ arcsec}^2$.

(Meurer et al. 2006). The observations were carried out on December 30, 2000, with an exposure time of 1800 s. The resolution of the $H\alpha$ image is equal to 1.5 arcsec. $H\alpha$ image of NGC 5474 was obtained by Knapen et al. (2004) on April 10, 2001, with an exposure of 1200 s and a seeing of 1.2 arcsec.

The absolute calibration of $H\alpha$ images were carried out using the descriptor parameters from the original FITS file and their explanations in Meurer et al. (2006) and Knapen et al. (2004).

Ultraviolet *Galaxy Evolution Explorer* (GALEX) *FUV* and *NUV* reduced images of NGC 895, NGC 5474, and NGC 6946 were downloaded from the B. A. Miculski Archive for space telescopes.⁴ The observations of NGC 895 were carried out on November 14, 2004, with a total exposure of 4869 s in every band. The observations of NGC 5474 were made on June 19, 2003, with a total exposure of 1610 s, the same in *FUV* and *NUV*. The observations of NGC 6946 were carried out on September 9, 2006. The total exposure time was 894.35 s in *FUV* filter and 3208.65 s in *NUV*. The image resolution is equal to 4.5 arcsec for *FUV* and 6.0 arcsec for *NUV*. The description of the GALEX mission, basic parameters of the passbands, files description, and data reduction were presented in Morrissey et al. (2005).

The *Spitzer Space Telescope InfraRed Array Camera* (IRAC) image of NGC 6946 in the $8\mu\text{m}$ band was retrieved as a FITS file from the NED database. It was obtained in the *SIRTF Nearby Galaxies Survey* (SINGS)⁵ (Kennicutt et al. 2003). The resolution of IRAC $8\mu\text{m}$ image is 2.4 arcsec. The observations of NGC 6946 were made on November 25, 2004 with an exposure of 2144 s. Data reduction of IRAC images is described in the IRAC Instrument

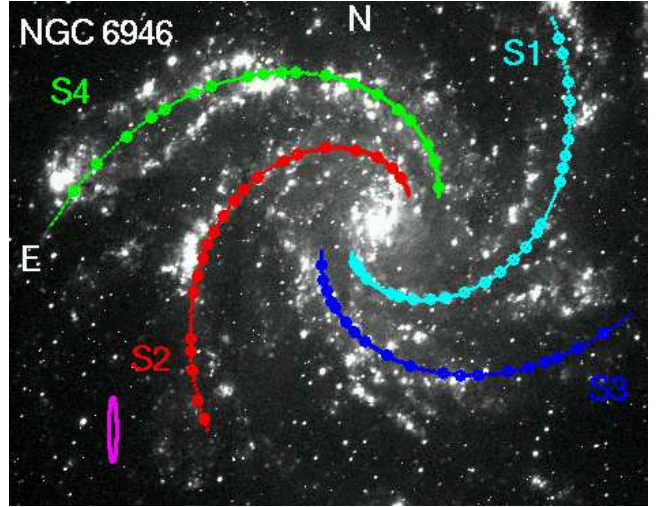


Figure 3. Same as Fig. 2, but for NGC 6946. Logarithmic spiral S4 is shown in green. The size of the used elliptical aperture is $50 \times 6 \text{ arcsec}^2$.

handbook⁶ (see also Elmegreen & Elmegreen 2019, and references therein).

2.2 Observations

UBVRI images of NGC 895 were obtained on October 10, 2004 with the 1.5 m telescope of the Maidanak Observatory (Ulugh Beg Astronomical Institute of the Uzbekistan Academy of Sciences) using a SITE-2000 CCD array. The focal length of the telescope is 12 m. Detailed description of the telescope, the CCD camera, and the filters is presented in Artamonov et al. (2010). With broad-band *U*, *B*, *V*, *R*, and *I* filters, the CCD array realizes a photometric system close to the standard Johnson–Cousins *UBVRI* system. The camera is cooled with liquid nitrogen. The size of the array is 2000×800 pixels. It provides the $8.9 \times 3.6 \text{ arcmin}^2$ field of view with the image scale of $0.267 \text{ arcsec pixel}^{-1}$. The seeing during the observations was 0.9–1.3 arcsec. The total exposure times were 900 s in *U* and *B*, 720 s in *V*, and 540 s in *R* and *I*.

Photometric *UBVRI* observations of NGC 5474 were made on June 22, 2009 with the same telescope with the SI-4000 CCD camera. The chip size, 4096×4096 pixels, provides a field of view of $18.1 \times 18.1 \text{ arcmin}^2$ with an image scale of $0.267 \text{ arcsec pixel}^{-1}$. The total exposure times were 1200, 600, 420, 360, and 240 s in the *U*, *B*, *V*, *R*, and *I* bands, respectively. The seeing was 1.2–1.8 arcsec.

2.3 Data reduction

The reduction of the photometric data was carried out using standard techniques, with the European Southern Observatory Munich Image Data Analysis System⁷ (ESO-MIDAS). The main image reduction stages for photometric data were as follows: correction for bias and flat field, removal of cosmic-ray traces, determining and subtracting the sky background, aligning and adding the images, removal of field stars, absolute calibration. The main photo-

⁴ <http://galex.stsci.edu/>

⁵ <http://irsa.ipac.caltech.edu>

⁶ <http://irsa.ipac.caltech.edu/data/SPITZER/docs/irac/iracinstrumenthandbook/>

⁷ <http://www.eso.org/sci/software/esomidas/>

Table 2. Parameters of logarithmic spiral arms in the galaxies.

NGC	Spirals	μ (degr)	r_0 (arcsec)	θ_0 (degr)
895	S1, S2	28.8 ± 0.8	5.75	270, 90
5474	S1	35.9 ± 2.8	5.62	90
	S2	15.3 ± 1.0	42.2	90
	S3	22.5 ± 0.4	57.2	90
6946	S1, S2	30.2 ± 1.2	32.0	135, 315
	S3, S4	31.0 ± 1.0	50.5	115, 295

metric *UBVRI* image reduction stages were described in detail in Gusev et al. (2016).

The absolute calibration of the photometric data involved reducing the data from the instrumental photometric system to the standard Johnson–Cousins system and correcting for the air mass using the derived colour equations and the results of the aperture photometry of the galaxies.

For the absolute calibration of NGC 895 data we derived the colour equations and corrected for atmospheric extinction using observations of photometric standards from the field of Landolt (1992) SA 98, carried out on the same night and on the same air mass in the *U*, *B*, *V*, *R*, *I* filters. A detailed study of the instrumental photometric system and the atmospheric extinction at the Maidanak Observatory was presented in Artamonov et al. (2010).

For the absolute calibration of NGC 5474 images the stars fields of Landolt (1992) PG 1657+078, SA 109, SA 110, and SA 111 were observed during the same set of observations in the wide air mass interval.

We also used the aperture photometric data for NGC 895 and NGC 5474 from the LEDA database for the absolute calibration of images of the galaxies.

At the final step, the images of the galaxies in all bands were transformed to the face-on position using the values of the inclination (*i*) and the position angle (PA) from Table 1. Those face-on images were used for the further analysis. Photometric magnitudes and fluxes were corrected for the Galactic extinction and for projection effects: $m_{\text{cor}} = m_{\text{obs}} - A_{\text{Gal}} - 2.5 \log(\cos(i))$ and $I_{\text{cor}} = I_{\text{obs}} 10^{0.4A_{\text{Gal}} \cos(i)}$.

3 RESULTS

3.1 Parameters of spiral arms

We investigate properties of spiral arms by curve fitting of spiral arms, which are clearly outlined in UV and blue optical (*U*, *B*) passbands (Figs. 1–3). The arms are defined by by-eye selection of pixels in the part of face-on *B* images that is within the spiral arms. Pixels in these regions are then fitted with a logarithmic spiral using linear least-squares.

A logarithmic spiral with a pitch angle μ is described as

$$r = r_0 e^{k(\theta - \theta_0)}, \quad (1)$$

where $k = \tan \mu$. We adopt two constraints for the fitting: (i) the pitch angle is constant along the arm, and (ii) the opposite spiral arms (S1 and S2 in NGC 895, S1 and S2, and S3 and S4 in NGC 6946) have the same values of μ and r_0 (Figs. 1, 3).

Results of the fitting are presented in Table 2. Remark that the obtained pitch angles for the arms in NGC 6946, $\mu = 30.2^\circ$ and 31.0° , are close to the results of Kendall, Clarke & Kennicutt

(2015) who obtained values $24.0^\circ \pm 0.6^\circ$, $29.3^\circ \pm 0.5^\circ$, and $29.5^\circ \pm 0.7^\circ$ using optical *V*, $3.6 \mu\text{m}$, and $4.5 \mu\text{m}$ images, respectively.

3.2 Along-arm photometry

For the further analysis, we used a technique developed by us in Gusev & Efremov (2013) and Gusev & Shimanovskaya (2020). To study brightness variations along spiral arms, we obtained photometric profiles of them. We used elliptical apertures with a minor axis along a spiral arm (a difference between PA of major axis and PA of the centre of aperture is a pitch angle), and a step of 1° by PA. The step used corresponds to the angular distance from 0.1 to 2 arcsec for spiral arms in NGC 895, from 0.1 to 3 arcsec for spiral arms in NGC 5474, and 0.6 to 4 arcsec for spiral arms in NGC 6946; it does not exceed the angular resolution in the *FUV* band.

The sizes of the apertures, $18 \times 3 \text{ arcsec}^2$ for NGC 895, $18 \times 4 \text{ arcsec}^2$ for NGC 5474, and $50 \times 6 \text{ arcsec}^2$ for NGC 6946, were selected taking into account the width of the spiral arms and characteristic sizes of star formation regions. The major axis was sized to cover all star formation regions in the spiral arms, but exclude regions outside of them. The size of the minor axis was chosen so that adjacent star formation regions were separated in photometric profiles. These apertures are plotted in Figs. 1–3.

Obtained photometric profiles in *FUV*, *U*, and *H α* along the arms of the galaxies are presented in Figs. 4–6, where the longitudinal displacement along the spiral, denoted as *s*, is

$$s = (\sin \mu)^{-1} r_0 (e^{k(\theta - \theta_0)} - 1) \quad (2)$$

for a logarithmic spiral in the form of Eq. (1). Additionally, we present $8 \mu\text{m}$ profiles along the spiral arms of NGC 6946 in Fig. 6.

Using the profiles in the *FUV* band and *H α* line, and involving profiles in the *U* band, we found the local brightness maxima on the profiles. We prefer to use the *FUV* and *H α* images that show the distribution of the young stellar population with ages of 1–10 Myr (*H α*) and 10–100 Myr (*FUV*). The *U* images were used for control.

The local maxima of brightness were determined as the lower extrema of the functions $m_{FUV}(s)$, $-\log F(H\alpha)(s)$ for the spiral arms. To locate them, we looked for points with the first derivative of the function, $dm_{FUV}/ds = 0$ or $d(\log F(H\alpha))/ds = 0$, and the second derivative, $d^2 m_{FUV}/ds^2 > 0$ or $d^2(-\log F(H\alpha))/ds^2 > 0$, on the profiles. We selected peaks whose widths exceed three measurement points (corresponding to the angular resolution of the images in optical bands) and whose amplitude exceeds the 3σ threshold above the average background level in the corresponding images of the galaxies within the used apertures (see dashed horizontal lines and open circles in Figs. 4–6).

The outer parts of the spiral arms S2 and S3 in NGC 5474 are faintly visible in the *H α* line. Due to the low signal-to-noise ratio, we excluded sections of profiles with $\log F(H\alpha) < -14.4$ from further consideration. The only *FUV* and *U* profiles were used for these sections (Fig. 5).

The local maxima of brightness found in both *FUV* and *H α* were taken as a single local maximum of brightness if the difference between their positions along the spiral arm, $|s_{FUV} - s_{H\alpha}|$, was less than the FWHM of the *FUV* peak profile and less than the FWHM of the *H α* peak profile.

The search for local maxima of brightness using the infrared $8 \mu\text{m}$ profiles of the spiral arms in NGC 6946 (Fig. 6) was carried out separately using the same algorithm.

As can be seen from Figs. 4–6, in a number of cases, the local maxima of brightness found from the *FUV* and *H α* profiles do not coincide with each other. This is a consequence of the fact

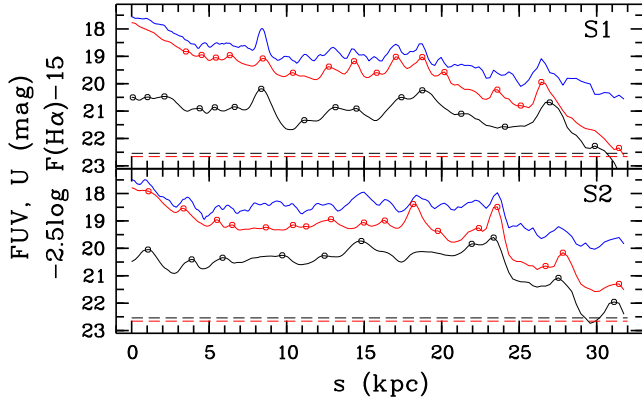


Figure 4. Photometric profiles in the U (blue), FUV (black) bands, and $H\alpha$ line (red) along the spiral arms S1 (top) and S2 (bottom) of NGC 895. The ordinate units are magnitudes and logarithm of $H\alpha$ flux in units of $\text{erg s}^{-1}\text{cm}^{-2}$ within the aperture. Positions of local maxima of brightness on the profiles in the FUV band (open black circles) and $H\alpha$ line (open red circles) are indicated. 3σ thresholds above the average background level for FUV (black) and $H\alpha$ images (red) are shown by dashed horizontal lines.

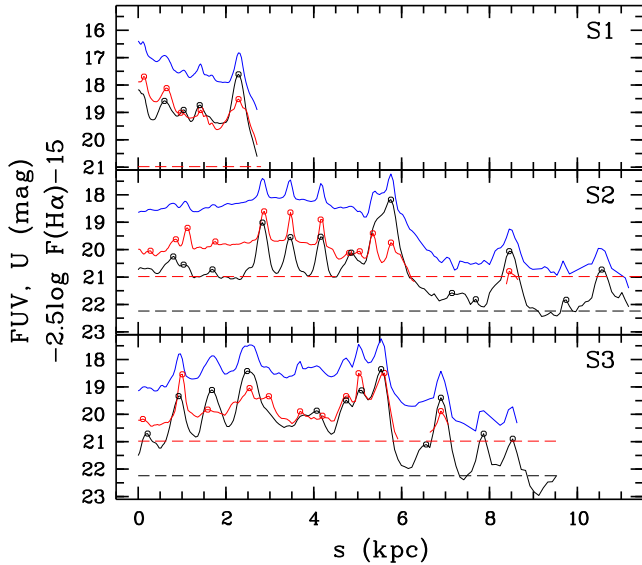


Figure 5. Photometric profiles in the U (blue), FUV (black) bands, and $H\alpha$ line (red) along the spiral arms S1 (top), S2 (middle), and S3 (bottom) of NGC 5474. Other symbols are the same as in Fig. 4.

that young stellar populations of different ages radiate in different wavelength ranges.

As a result, we obtained 23 local maxima of brightness in the spiral arm S1 and 18 local maxima of brightness in the spiral arm S2 of NGC 895 (Fig. 4); 5, 13, and 13 local maxima of brightness in the spiral arms S1, S2, and S3 of NGC 5474, respectively (Fig. 5); 25, 21, 19, and 19 local maxima of brightness in the spiral arms S1, S2, S3, and S4 of NGC 6946, respectively (Fig. 6). Analysis of infrared $8\mu\text{m}$ profiles of NGC 6946 gave 17 local maxima of brightness for the spiral arms S1 and S3, and 16 local maxima of brightness for the spiral arms S2 and S4 (Fig. 6).

The typical errors of maximum positions are $\Delta s = 1$ measure-

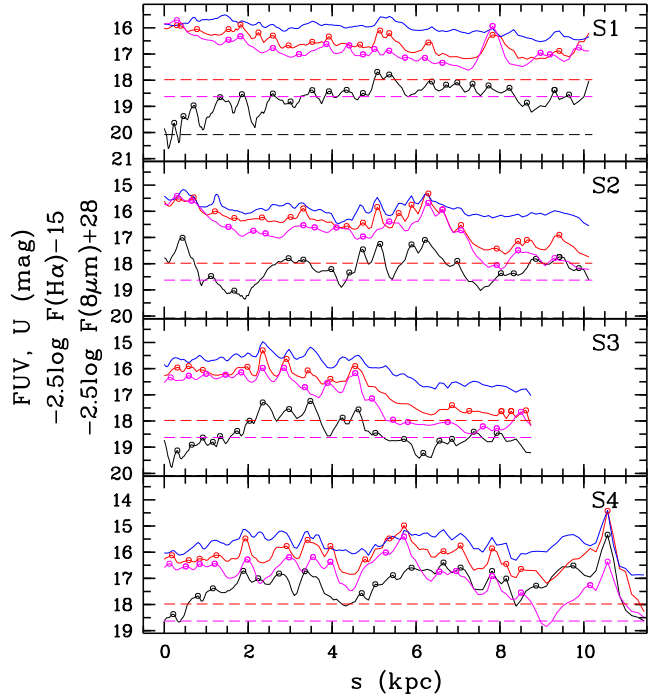


Figure 6. Photometric profiles in the U (blue), FUV (black) bands, $H\alpha$ line (red), and $8\mu\text{m}$ (magenta) along the spiral arms S1–S4 of NGC 6946. $8\mu\text{m}$ flux is given in units of Jy within the aperture. Positions of local maxima of brightness on the profiles in the $8\mu\text{m}$ IRAC band are indicated by open magenta circles. The 3σ threshold above the average background level for the $8\mu\text{m}$ image is shown by the magenta dashed horizontal line. Other symbols are the same as in Fig. 4.

ment points. Taking into account the linear resolution of the $H\alpha$ images of galaxies, mean positions errors are equal to ± 150 pc for NGC 895, ± 20 , ± 30 , and ± 40 pc for the arms S1, S2, and S3 of NGC 5474, respectively, ± 40 pc for the spirals S1, S2, and S3 in NGC 6946, and ± 50 pc for the spiral arm S4 of NGC 6946 (see error bars in Fig. 7). Individual uncertainties for the identified local maxima of brightness are presented in Table A1.

In the next step, we measured separations, l , between adjacent local maxima of brightness along the spiral arms in the galaxies. Separation, l , between $(n-1)$ -st and n -th local maxima of brightness is defined as $l_n = s_n - s_{n-1}$, where $s \equiv s_n$ is defined from Eq. (2). Distribution of the local maxima of brightness by separation l in the arms of galaxies is presented in Fig. 7. Numerical values of s , l , and galactocentric distances r for the local maxima of brightness and their pairs are presented in Table A1.

The obtained separations are larger, with a few exceptions, than a linear resolution of the FUV images (700 pc for NGC 895, 150 pc for NGC 5474, and 130 pc for NGC 6946). Several measurements with smaller separations are confirmed by $H\alpha$ profiles along the spiral arms. Linear resolutions of the $H\alpha$ images (240 pc for NGC 895, 40 pc for NGC 5474, and 30 pc for NGC 6946), as well as $8\mu\text{m}$ image linear resolution for NGC 6946 (70 pc) are significantly smaller than minimum values of l (see Figs. 7, 8).

As we noted above, FWHMs of the peak profiles exceed the linear resolutions of the $H\alpha$ and optical images of the galaxies in all cases.

Photometric profiles along spiral arms in Figs. 4–6 cannot be

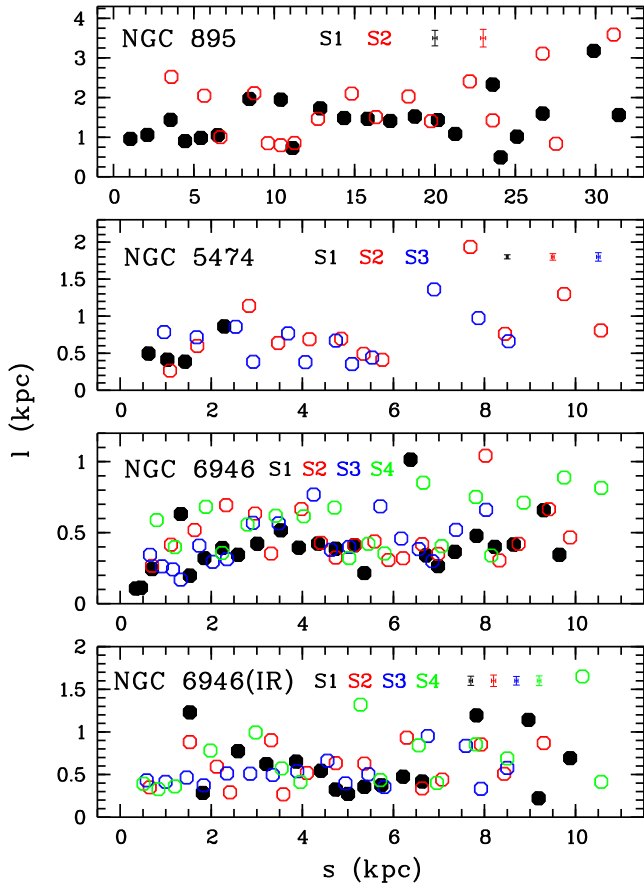


Figure 7. Separations l between adjacent local maxima of brightness along the spiral arms of NGC 895, NGC 5474, and NGC 6946 from the UV and optical data (three top panels) and along the spiral arms of NGC 6946 from the IR data (bottom panel). Separations l along arms S1–S4 are indicated by black, open red, open blue, and open green circles, respectively. The mean error bars are shown. See the text for details.

used directly for estimating photometric parameters of individual young star clusters and complexes because of highly elliptical apertures used to obtain them. Several star clusters and H II regions may be found to be in the measured area due to the large major axis. On the other hand, the size of the minor axis, 3–6 arcsec, is smaller than angular sizes of large star complexes. Peak H α fluxes and FUV magnitudes may be used for measuring photometric fluxes of star formation regions only for compact separate H II regions and star clusters.

We estimated star formation rates of star formation regions in the galaxies using their H α luminosities and FUV absolute magnitudes with the conversion factor of H α luminosity to star formation rate of Kennicutt (1998):

$$\text{SFR}(M_{\odot} \text{ yr}^{-1}) = 7.9 \cdot 10^{-42} L(\text{H}\alpha)(\text{erg s}^{-1})$$

and the conversion factor of FUV luminosity to star formation rate of Iglesias-Páramo et al. (2006) in the form

$$\text{SFR}(M_{\odot} \text{ yr}^{-1}) = 7.0 \cdot 10^{-8} \cdot 10^{-0.4M_{FUV}}.$$

Photometric luminosities and fluxes were corrected for the extinction due inclination effects (see Table 1).

We roughly (to the order of magnitude) estimated masses of

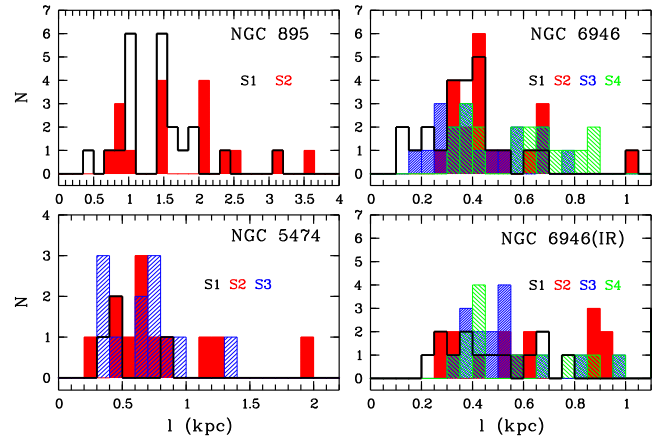


Figure 8. The number distribution histograms of local maxima of brightness by separation between adjacent objects along the spiral arms of NGC 895 (top-left), NGC 5474 (bottom-left), NGC 6946 (top-right) obtained from the UV and optical data, and along the spiral arms of NGC 6946 obtained from the IR data (bottom-right). The colours of the curves corresponding to the various spiral arms are the same as in Fig. 7. See the text for more explanation.

the young star clusters, assuming that a character time scale of star formation in OB associations and star complexes is ~ 10 Myr (Efremov & Elmegreen 1998). More precise mass estimates require more detailed analysis of photometric and spectral parameters and are beyond the scope of this study.

3.3 Analysis of the spatial distribution of local maxima of brightness

We built histograms of the distribution of separations l in the spiral arms of the galaxies (Fig. 8). In addition, we decided to perform the Fourier analysis to search for characteristic separations between local maxima of brightness.

Observational data are often noisy and unevenly spaced both in the time domain and in the spatial domain. Therefore the direct use of the Fourier analysis to investigate periodicities in those data can be rather problematic. The normalized periodogram was initially defined by Scargle (1982) to estimate the power spectrum for unevenly sampled time series. We use the modified periodogram method of Horne & Baliunas (1986) for spatial data series of separations l between local maxima of brightness in the spiral arms of the galaxies. To estimate the significance of the height of a peak in the power spectrum, the concept of the false alarm probability (FAP) was adopted (Scargle 1982). The FAP characterizes the probability that a peak of a certain height or higher will occur, assuming that the data are pure noise. An important parameter for the calculation of the FAP is the number of independent frequencies N from $\omega_0 = 2\pi/L$ to $\omega_N = \pi N_0/L$, where L is the largest separation, N_0 is the number of data points in the initial data series. Through simulation of a large number of data sets, Horne & Baliunas (1986) empirically derived the formula for N :

$$N = -6.362 + 1.193N_0 + 0.00098N_0^2.$$

This formula is accurate for evenly spaced data but it overestimates the number of independent frequencies for unevenly sampled data. Therefore false alarm probabilities for the unevenly sampled data, as in our study, could be significantly smaller.

So we computed the Lomb-Scargle periodograms, using the technique developed by Scargle (1982), Horne & Baliunas (1986), and Press & Rybicki (1989), and also thoroughly explained in VanderPlas (2018), for our data to estimate the power spectrum. For this, we used functions $D(s)$, $D_n(s)$, $p(s)$, and $p_n(s)$. The function $D(s) = 1$ in points of the local maximum of brightness and $D(s) = 0$ in all other points. The function $D_n(s)$ is a function $D(s)$ normalized to the maximum amplitude of FUV or $H\alpha$ peak. The function $p(s)$ is a collection of Gaussians, centered at points of local maxima of brightness on the profiles, with σ equal to the peak positioning error. The function $p_n(s)$ is a function $p(s)$ with the Gaussian amplitudes normalized to the maximum amplitude. If significant peaks were recorded in both bands (FUV and $H\alpha$), the largest normalized amplitude was adopted. Outside of the Gaussians, the functions $p(s)$ and $p_n(s) = 0$ for all other points.

An analysis of the periodograms for the functions $D(s)$, $D_n(s)$, $p(s)$, $p_n(s)$ showed that they all have peaks at the same l (for each individual spiral arm), but with slightly different power spectral density (PSD) values. In Fig. 9 we present the periodograms for the function $p(s)$.

In Gusev & Efremov (2013) and Gusev & Shimanovskaya (2020) we showed that the Fourier analysis of raw intensity profiles reveals only long-scale regularities. It is not sensitive to the short-scale regularities which are of interest to us. So we do not show periodograms calculated directly for unmodified deprojected intensities along the arms in FUV and $H\alpha$ in Fig. 9.

Because we have different numbers of local maxima of brightness N_0 for different spiral arms in NGC 895, NGC 5474, and NGC 6946, numbers of independent frequencies N differ too, and therefore normalized periodograms in Fig. 9 have different smoothness.

Power spectral density (ordinate axis) in Fig. 9 is normalized to the PSD with a false-alarm probability (FAP; see Horne & Baliunas 1986, for details) equal to 25%.

Below, we consider the distribution of star formation regions along the spiral arms separately for each spiral arm.

3.3.1 NGC 895

For NGC 895, Elmegreen & Elmegreen (1983) found a regular chain of HII regions in S1, consisting of six objects with a separation of about 1.4 kpc (Fig. 1). All regions of Elmegreen & Elmegreen (1983) are identified by us as local maxima of brightness. They are located at the longitudinal displacement $s = 8 - 20$ kpc (galactocentric distances $r = 4.8 - 10.5$ kpc; see Figs. 4, 7). Figure 7 shows a rather regular separation between adjacent local maxima of brightness along the S1 with separations $l \approx 1$ kpc at $s = 0 - 7$ kpc ($r = 0.9 - 4.3$ kpc) and $l \approx 1.5$ kpc at $s = 13 - 20$ kpc ($r = 7.2 - 10.5$ kpc). The difference between separations found by Elmegreen & Elmegreen (1983) and ourselves is explained, firstly, by different adopted values of the distance and inclination of the disc of NGC 895, and, secondly, by the fact that we found more local maxima of brightness than Elmegreen & Elmegreen (1983) in the same segment of the spiral arm (see Fig. 1). We also note that all distances between adjacent local maxima of brightness are a multiple of 0.5 kpc with an accuracy of $\pm 10\%$. The exception is a trio of regions at $s = 11 - 13$ kpc ($r = 6.2 - 7.2$ kpc) with distances of 0.7 and 1.7 kpc and a pair of regions at $s = 23.5$ kpc ($r = 12.2$ kpc) with a distance of 2.3 kpc (Fig. 7).

Distribution of star formation regions in the S1 by separations have two clear peaks at $l \approx 1$ kpc and $l \geq 1.5$ kpc (Fig. 8). The dis-

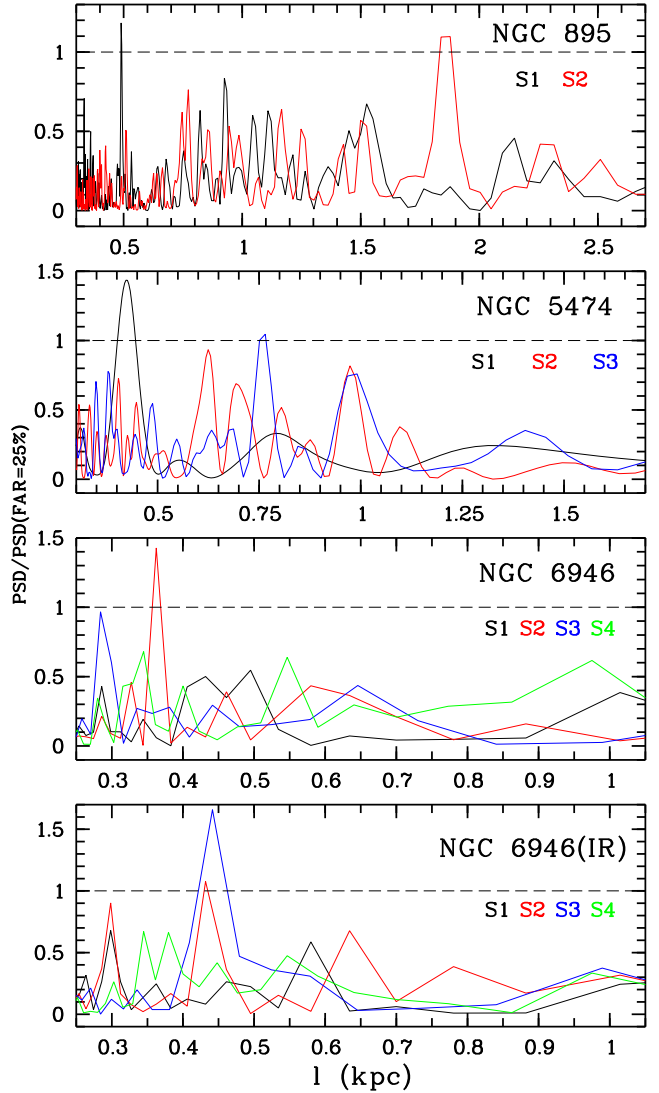


Figure 9. Normalized power spectral density of the function $p(s)$ for the spiral arms in NGC 895, NGC 5474, and NGC 6946 from the UV and optical data, and for the spiral arms of NGC 6946 from the IR data. The colours of the curves corresponding to the various spiral arms are the same as in Fig. 7. See the text for more explanation.

tribution of separations can be bimodal. Given the sample size is too small to make a robust multimodality test, we calculated distances D between the peaks relative to their widths according to the definition by Ashman, Bird & Zepf (1994): $D = |\mu_a - \mu_b| / \sqrt{(\sigma_a^2 + \sigma_b^2)/2}$, where μ_a , μ_b are the means of subsets a and b , σ_a , σ_b are the standard deviations, which include the intrinsic measurement errors in pairs, ± 200 pc. As is known, $D > 2$ is required for a clean separation between the modes. We selected two subsets. The first one includes seven pairs with separations from 0.9 to 1.1 kpc, and the second one includes eight pairs with separations from 1.4 to 1.6 kpc. The mean separations in the subsets are 1.01 ± 0.20 kpc and 1.49 ± 0.22 kpc, which gives $D = 2.32$ and testifies in favour of a bimodal distribution of separations.

The periodogram shows a noticeable peak with a FAP $< 20\%$ at $l = 490$ pc for the S1 (Fig. 9). Weak additional peaks at separations ≈ 1 kpc and ≈ 1.5 kpc have a FAP $> 30\%$. But we should

remember that the significance of a peak in the periodogram is underestimated in the case of unevenly sampled data.

Elmegreen & Elmegreen (1983) did not find any regularity in distribution of H II regions in the spiral arm S2 of NGC 895. Our analysis shows the presence of regularities with scales of ~ 1 , ~ 1.5 , and ~ 2 kpc, including a chain of four star formation regions with $l = 840$ pc at $s = 9 - 12$ kpc ($r = 5.2 - 6.7$ kpc; Fig. 7).

These three characteristic scales are confirmed by the corresponding peaks in the histogram in Fig. 8. The mean separations in these three subsets, corresponding to the pairs with separations of ~ 1 , ~ 1.5 , and ~ 2 kpc, are 0.87 ± 0.23 , 1.45 ± 0.21 , and 2.07 ± 0.20 kpc, including the intrinsic errors. The parameter D is equal to 2.65 for subsets with $l \sim 1$ and ~ 1.5 kpc, and 3.02 for subsets with $l \sim 1.5$ and ~ 2 kpc. At the same time, the periodogram has a single significant peak with a FAP < 25% at $l = 1.85 - 1.9$ kpc (Fig. 9). We remark that the characteristic separations, found in the S2, are multiples of 500 pc, as in the S1 arm.

The brightest and largest H II regions in the galaxy are located in S2 at $s = 18$ and 24 kpc (Fig. 4). Their sizes, 600-650 pc, are typical for star complexes. Luminosities of these complexes in H α reach $9.1 \cdot 10^{39}$ erg s $^{-1}$ which corresponds to SFR = $0.07 M_{\odot}$ yr $^{-1}$ and $m \sim 7 \cdot 10^5 M_{\odot}$. The brightest H II regions in the opposite arm, S1, at $s = 8.5$ and 18 kpc (Fig. 4) are fainter. Their H α luminosity is equal to $4.0 \cdot 10^{39}$ erg s $^{-1}$, SFR = $0.03 M_{\odot}$ yr $^{-1}$, and $m \sim 3 \cdot 10^5 M_{\odot}$. The faintest H II regions, detected in the profiles in Fig. 4 in the galaxy, have $L(\text{H}\alpha) = 1.2 \cdot 10^{38}$ erg s $^{-1}$, SFR = $0.001 M_{\odot}$ yr $^{-1}$, and $m \sim 9 \cdot 10^3 M_{\odot}$.

The brightest young star complexes in *FUV* are also systematically brighter in S2 arm than in S1. The two brightest complexes with $M_{FUV} = -14.40$ mag are located at $s = 15$ and 24 kpc (Fig. 4). Their SFRs and masses, $0.07 M_{\odot}$ yr $^{-1}$ and $\sim 7 \cdot 10^5 M_{\odot}$, turned out to be the same as those calculated from the H α luminosity. We note that the star complex at $s = 15$ kpc, which is the brightest in the *FUV*, is not distinguished by the H α emission (Fig. 4).

In contrast to the sample of star formation regions in S2, all star complexes in S1, that are bright in *FUV*, are powerful H II regions. The estimates of SFRs, $0.016 M_{\odot}$ yr $^{-1}$, and masses, $\sim 1.6 \cdot 10^5 M_{\odot}$, of the brightest star complexes in *FUV* in S1 with $M_{FUV} = -12.76$ mag are slightly smaller than ones obtained from the H α data.

The faintest young star clusters, visible in *FUV* band, have $M_{FUV} \approx -11.1$ mag, which corresponds to SFR = $0.0035 M_{\odot}$ yr $^{-1}$ and $m \sim 3.5 \cdot 10^4 M_{\odot}$. Higher minimal SFR detected in *FUV* than in H α is due to the lower resolution and signal-to-noise ratio of *FUV* observations.

Masses of the brightest star complexes in NGC 895 are close to masses of the largest complexes in giant late type galaxies, such as M51, where the mass of the largest star formation complex is $\sim 3 \cdot 10^5 M_{\odot}$ (Larsen et al. 2001), and NGC 6946, with the most massive stellar complex of $\sim 8 \cdot 10^5 M_{\odot}$ (Bastian et al. 2005).

3.3.2 NGC 5474

Only five local maxima of brightness were found in the inner short spiral arm of NGC 5474 (S1; see Figs. 2, 5). The first four of them form a regular chain with a separation 430 ± 60 pc, and the distance between the fourth and fifth local maxima of brightness is twice as large and equal to 860 ± 30 pc (Figs. 7, 8). The Fourier analysis of a sample of five objects can only be formal; it shows the selected scale of 420 pc with a FAP < 15% (Fig. 9).

Distribution of star formation regions in S2 looks rather irregular (Figs. 7, 8). Some regularity seems to be observed in the inner

part of this spiral arm at $s = 1.5 - 5$ kpc ($r = 1.8 - 2.7$ kpc), where we found six local maxima of brightness. Five of them are located at a distance 660 ± 60 pc from each other, and one pair has a double separation $l = 1.14 \pm 0.05$ kpc (Fig. 7). The four most distant star formation regions from this sample were identified by Elmegreen & Elmegreen (1983) as a regular chain of four H II regions (see Fig. 2).

Power spectral density of the function $p(s)$ for S2 never reaches the level of 25% FAP. The PSD maximum at $l \approx 620$ pc probably reflects the fact of quasi-regularity in distribution of star formation regions at $s = 1.5 - 5$ kpc in the S2 arm (Fig. 9).

Unlike the S2, the spiral arm S3 in the galaxy shows a regular distribution of the young stellar population along the arm. Two characteristic separations are stand out in the S3. We found four pairs of adjacent local maxima of brightness with a separation of $l = 390 \pm 70$ pc and six pairs with a spacing of $l = 740 \pm 90$ pc (Figs. 7, 8). The bimodal separation distribution is confirmed by the value of the parameter $D = 4.34$. The spectrum of the function $p(s)$ for S3 also confirms the characteristic distance of 750 pc with a FAP = 25% (Fig. 9). This scale was noted in Elmegreen & Elmegreen (1983).

Note that the H α -to-*FUV* surface brightness ratio along the spiral arms is systematically lower in NGC 5474 than in NGC 895 and NGC 6946 (compare Figs. 4-6). This is especially noticeable for arms S1 and S3 (Fig. 5). Apparently, this is a consequence of the relative deficit of H $_2$ in the less-massive NGC 5474.

The sizes of the largest H II regions, observed in the galaxy, are 200-250 pc. The brightest star formation regions are located in the inner spiral arm S1 at $s = 1.5$ and 2.4 kpc (Fig. 5). Their $L(\text{H}\alpha) = 5.1 \cdot 10^{38}$ erg s $^{-1}$ and $M_{FUV} = -12.72$ mag. These values correspond to SFR = $0.004 M_{\odot}$ yr $^{-1}$ and $m \sim 4 \cdot 10^4 M_{\odot}$ by H α luminosity and SFR = $0.009 M_{\odot}$ yr $^{-1}$ and $m \sim 9 \cdot 10^4 M_{\odot}$ by *FUV* absolute magnitude.

Outer spiral arms S2 and S3 contain star formation regions with $L(\text{H}\alpha) \leq 3.0 \cdot 10^{38}$ erg s $^{-1}$ and $M_{FUV} \geq -11.80$ mag which correspond to SFR = $0.002 - 0.004 M_{\odot}$ yr $^{-1}$ and $m \sim (2 - 4) \cdot 10^4 M_{\odot}$. The brightest ones are located at $s = 2.9, 3.5, 4.1$, and 5.5 kpc in S2, and at $s = 5.0$ and 5.5 kpc in S3 (Fig. 5). Note that the bright *FUV* source at $s = 5.5$ kpc in S2 does not emit in H α . In spite of the similar SFRs (masses) of the brightest star formation regions in S2 and S3 arms, young regions in S2 are more compact. Their diameters are ≤ 150 pc.

Smaller maximal masses of star formation regions in NGC 5474 as compared with NGC 895 and NGC 6946 are a consequence of the smaller total mass of NGC 5474 and the smaller fraction of the molecular hydrogen in it as compared to the giant galaxies NGC 895 and NGC 6946.

The faintest star formation regions, derived from the *FUV* and H α images, have $L(\text{H}\alpha) \approx 1.6 \cdot 10^{37}$ erg s $^{-1}$ and $M_{FUV} \approx -9.0$ mag. SFR in them is equal to $1 \cdot 10^{-4} M_{\odot}$ yr $^{-1}$ ($m \sim 1 \cdot 10^3 M_{\odot}$) based on H α data and $2.5 \cdot 10^{-4} M_{\odot}$ yr $^{-1}$ ($m \sim 3 \cdot 10^3 M_{\odot}$) based on *FUV* luminosity.

3.3.3 NGC 6946

Most of spiral arms in NGC 6946 look ragged. The only exception is the spiral arm S2 (Fig. 3). It would be hard to expect an accurate regularity in distribution of star formation regions here.

Spatial distribution of local maxima of brightness in the spiral arm S1 does not show a certain characteristic separation. However, most of the pairs, 13 out of 24, have separations in a narrow range of 320-420 pc (Figs. 7, 8). Among them, we can distinguish a regular

chain of five star formation regions at $s = 3.5 - 5.2$ kpc ($r = 2.7 - 3.5$ kpc) with a spacing of 400 ± 60 pc (Fig. 7).

The distribution of infra-red sources in S1 looks even more chaotic, although all distances between adjacent regions lie in the same range of separations as found in optics and UV (see right panels in Fig. 8).

Local maxima of brightness, detected in UV and $H\alpha$, are distributed in the spiral arm S2 rather regularly. 13 pairs out of 20 have separations from 310 to 470 pc with a mean $l = 380 \pm 85$ pc (Figs. 7, 8). This scale is confirmed by the Fourier analysis: the periodogram shows a strong peak at $l = 360$ pc with a FAP $< 15\%$ (Fig. 9).

Distribution of regions of incipient star formation visible in $8\mu\text{m}$ shows stronger spatial regularity in S2 than the distribution of star formation regions visible in UV and $H\alpha$ line (Fig. 7). Three separations were found for pairs of IR sources: 310 ± 65 , 555 ± 95 , and 890 ± 70 pc (Fig. 8). Segregation of the subsets is confirmed by the value of parameter D , which is equal to 3.01 for subsets with $l \sim 300$ and $l \sim 550$ pc, and is equal to 4.01 for subsets with $l \sim 550$ and $l \sim 900$ pc. Note that both larger scales are multiples of the smallest scale 300 pc.

Power spectral density of the function $p(s)$ for IR sources in S2 reaches its maximum at $l = 300$ and 430 pc with a FAP $\approx 25\%$ (Fig. 9). The first maximum coincides with the smallest scale. The second maximum lies between scales of ~ 300 and ~ 550 pc. The discrepancy between the scales obtained using the Fourier analysis and those found from the histogram is apparently due to the absence of regular chains of star formation regions in S2. There are no adjacent pairs with the same separation in this arm (Fig. 7).

Distribution of star formation regions, visible in optics and UV in the spiral arm S3, is similar to those in the inner arms S1 and S2 (Fig. 8). More than a half of pairs have separations from 240 to 410 pc with a mean $l = 330 \pm 80$ pc. This spacing scale is similar to the result of the Fourier analysis: PSD reaches a maximum at 280 pc with a FAP $\approx 25\%$ (Fig. 9).

We observe two regular chains of IR sources in the inner part of S3. The first four pairs at $s = 0.5 - 2$ kpc ($r = 1.2 - 2.4$ kpc) have a separation $l = 420 \pm 60$ pc, and the second four pairs at $s = 2.4 - 4$ kpc ($r = 2.7 - 3.5$ kpc) have a separation $l = 515 \pm 50$ pc (Fig. 7). The regularity in the distribution of IR sources is lost in the outer parts of the spiral arm. In general, two characteristic scales of separations can be distinguished along the spiral arm, seven pairs with l in the range of 330 – 460 pc and six pairs with spacings from 500 to 580 pc (Fig. 8). However, these subgroups do not segregated by the criterion of Ashman et al. (1994): with average values of 395 ± 70 and 520 ± 65 pc, a parameter $D = 1.86$. Note that, as in the case of the spiral arm S2 of the galaxy, the periodogram shows a significant peak with a FAP $< 15\%$ at $l = 440$ pc, in the middle of two subsets (Fig. 9).

Histograms in Fig. 8 have peaks in the distribution of star formation regions by separation in the brightest spiral arm of NGC 6946, S4, at $l \approx 400$ pc for both UV- $H\alpha$ and IR sources. The distances between seven pairs of adjacent UV and $H\alpha$ emission regions lie in a narrow range of 320 – 420 pc with a mean $l = 370 \pm 75$ pc. All other pairs have separations $l \geq 560$ pc. Among the wide pairs, we suspect a slow increase in the typical separation l with the galactocentric distance r (see Fig. 7).

The distribution of IR sources along the S4 arm completely coincides with the distribution of UV- $H\alpha$ regions. Seven close pairs with separations of 330 – 430 pc have a mean $l = 390 \pm 70$ pc. Wide pairs have spacings $l \geq 570$ pc. At the same time, the periodograms do not show any significant peaks at 300 – 400 pc (see Fig. 9).

As in NGC 895, we observe an asymmetry of distribution of

young stellar population in the disc of NGC 6946. The star formation is more active in the eastern spiral arms S2 and S4 (Fig. 3). The brightest source of modern star formation is located on the end of S4 at $s = 10.5$ kpc (Fig. 6). It has $L(H\alpha) = 6.8 \cdot 10^{39}$ erg s $^{-1}$ and $M_{FUV} = -13.79$ mag, which corresponds to SFR = $0.054 M_{\odot}$ yr $^{-1}$ from $H\alpha$ data and 0.023 from FUV data. The mass of this region, $\sim (2 - 5) \cdot 10^5 M_{\odot}$, is close to the mass of the brightest star complex in NGC 895.

The brightest star formation regions in S2, located in a chain at $s = 4.5 - 7.0$ kpc (Fig. 6), are approximately twice as faint and less massive than those in S4. The brightest star formation regions in the western spiral arms S1 at $s = 5.1$ kpc and S3 at $s = 2.4 - 4.6$ kpc reach $H\alpha$ luminosities $1.4 \cdot 10^{39}$ erg s $^{-1}$ and FUV absolute magnitudes -11.20 . Their SFR, estimated using $H\alpha$ and FUV data, are equal to $0.010 M_{\odot}$ yr $^{-1}$ ($m \sim 1 \cdot 10^5 M_{\odot}$) and $0.002 M_{\odot}$ yr $^{-1}$ ($m \sim 2 \cdot 10^4 M_{\odot}$), respectively.

The faintest star clusters and H II regions, detectable in the galaxy with $L(H\alpha) \approx 4.2 \cdot 10^{37}$ erg s $^{-1}$ and $M_{FUV} \approx -9.9$ mag, have SFR = $4 \cdot 10^{-4} M_{\odot}$ yr $^{-1}$ and $m \sim 4 \cdot 10^3 M_{\odot}$ from $H\alpha$ measurements and SFR = $7 \cdot 10^{-4} M_{\odot}$ yr $^{-1}$ and $m \sim 7 \cdot 10^3 M_{\odot}$ from FUV measurements.

The most massive star complex in the galaxy, with a diameter of 600 pc and a mass of up to $8 \cdot 10^5 M_{\odot}$ (Bastian et al. 2005), is located in the disc in the middle of S1 and the end of S3; therefore, it was not included in our study. This is the brightest FUV source ($M_{FUV} = -14.06$ mag), but in the $H\alpha$ line it looks like a group of weak H II regions located along the edges of the complex (Fig. 3). This is due to its age, 15 Myr (Bastian et al. 2005).

4 DISCUSSION

Our analysis of the spatial distribution showed that in most spiral arms of NGC 895 and NGC 5474 there is a regularity in the distribution of star formation regions along the spiral arms of the galaxies. In the arm S2 of NGC 5474, where no characteristic regularity scale has been found, there is a regular chain consisting of several star formation regions. In the case of NGC 6946, we could rather talk about a quasi-regularity in the spatial distribution of star formation regions. The spacings between adjacent regions lie in a narrow range; however, regular chains are not observed in all spiral arms, except for S2.

Thus, the presence of a characteristic scale of distances between adjacent star formation regions along spiral arms seems to be more common than previously thought. The absence of strong regularity in three of four spiral arms of NGC 6946 can be explained by their morphology. In S1 and S4, the parallel chains of star formation regions are observed along the outer and inner edges of the spiral arms; spiral arm S3 branches into several segments (Fig. 3). Such structures might blur a possible spatial scale in the distribution of star formation regions.

We note that in spiral arms where several characteristic separations are found, the larger ones are multiples of the smallest one. At the same time, the smallest separations $l \sim 350 - 500$ pc in most spiral arms are close to the characteristic spacings obtained earlier for NGC 628, NGC 6217, and M100 (Gusev & Efremov 2013; Elmegreen et al. 2018; Gusev & Shimanovskaya 2020). In the distant galaxy NGC 895, the characteristic separations are multiples of ~ 500 pc, however, our angular resolution does not allow us to study the galaxy at this scale. We encountered a similar situation earlier when analysing the spatial regularity in the distant galaxy NGC 6217 (Gusev & Shimanovskaya 2020).

We attempted to apply the criterion of the gravitational instability of the gaseous, stellar-gaseous and multicomponent disc (Safronov 1960; Elmegreen & Elmegreen 1983; Jog & Solomon 1984a,b; Romeo & Falstad 2013; Rafikov 2001) for numerical calculations of the observed scale of regularities in the distribution of the young stellar population in spiral arms. Calculations of the perturbation wavelength in the disc of NGC 628, in which regular chains of star formation regions with a characteristic spacing of ≈ 400 pc are observed (Gusev & Efremov 2013), and in the disc of NGC 6946 based on modern data on surface density and velocity dispersions of atomic and molecular hydrogen and of the disc stellar population (projects *THINGS*⁸ (Walter et al. 2008), *BIMA SONG*⁹ (Helfer et al. 2003), *HERACLES* (Leroy et al. 2009), *SINGS* (Kennicutt et al. 2003); see the detailed technique in Leroy et al. 2008) predict characteristic separations between adjacent star formation regions of the order of several kiloparsecs, provided that the parameters are averaged over scales larger than the instability wavelength. This is well illustrated by the instability wavelength map in NGC 628 (fig. 4 in Marchuk 2018). At the same time, an approximate constancy of the surface density and velocity dispersion of atomic and molecular hydrogen and of the disc stellar population is indeed observed in NGC 628 and NGC 6946 in the range of galactocentric distances, where regularity in the distribution of star formation regions was found. Approximate constancy of the H I density is also observed in a wide range of galactocentric distances in NGC 5474 (Rownd et al. 1994; Pascale et al. 2021). As we noted in Introduction, fragmentation calculations for gaseous filaments and multicomponent spiral arms (Inutsuka & Miyama 1997; Mattern et al. 2018; Inoue & Yoshida 2018) also predict a regularity scale larger than 1 kpc for NGC 628 (Inoue et al. 2021). Thus, current theoretical approaches cannot adequately explain the sub-kiloparsec regularity scale in the distribution of the young stellar population along the spiral arms.

We have not found any noticeable difference in the distribution of star formation regions with an age of 3 – 100 Myr, visible in the UV and optics, and younger star formation regions, visible in the IR, in NGC 6946.

A magnetic field in a galaxy can change instability conditions and parameters, such as instability growth time and wavelength (Elmegreen & Elmegreen 1983). It can stabilize and freeze the initial spatial regularities, if they exist. For example, a regular magnetic field with a wavelength of 2.3 kpc was found by Beck et al. (1989) in the same arm segment of M31 in which Efremov (2009, 2010) noticed a regular string of star complexes with a spacing of 1.1 kpc.

Frick et al. (2000) found that the magnetic arms in NGC 6946, visible in polarized radio emission at 3.5 and 6.2 cm, are localized almost precisely between the optical arms; and each magnetic arm is similar in length and pitch angle to the preceding optical arm. The regions of maximum polarized intensity in the galaxy are located near the inner parts of optical spiral arms S1 and S2, and near the middle part of the S3 arm. It is in these parts of the spiral arms that we have not found regular chains of star formation regions (see Fig. 7). On the other hand, the ratio of the excess in the regular magnetic field over the azimuthal average at 3.5 cm in the arms turns out to be maximum at galactocentric distances of 3–6 kpc (see fig. 7 in Frick et al. 2000). It is at these galactocentric distances, that

regular chains of star formation regions, consisting of 3 – 5 objects, are observed in most spiral arms of NGC 6946.

5 CONCLUSIONS

We found a spatial regularity or quasi-regularity in the distribution of star formation regions along arms and (or) regular chains of star formation regions consisting of 3 – 5 objects in all spiral arms of galaxies studied in this paper. It is worth noting that these three galaxies have noticeably different structural features.

The obtained characteristic separations between adjacent star formation regions are from 350 to 500 pc or (and) multiples of them in the majority of spiral arms. The larger characteristic separations are multiples of the smallest one in those spiral arms where several characteristic separations are observed.

The characteristic scales of 350–500 pc obtained in NGC 895, NGC 5474, and NGC 6946 are close to those found earlier in NGC 628, M100, and NGC 6217.

ACKNOWLEDGMENTS

We are grateful to the anonymous referee for his/her constructive comments. The authors acknowledge the use of the HyperLeda data base (<http://leda.univ-lyon1.fr>), the NASA/IPAC Extragalactic Database (<http://ned.ipac.caltech.edu>), Barbara A. Miculski Archive for space telescopes (<https://archive.stsci.edu>), the H I Nearby Galaxy Survey (THINGS) data archive (<http://www.mpia.de/THINGS>) and the IDL Astronomy User's Library (<https://idlastro.gsfc.nasa.gov>). The authors would like to thank *SINGG*, *GALEX*, *SINGS*, *THINGS*, *BIMA SONG*, *HERACLES*, and the project of Knapen et al. (2004) teams for making observational data available. This study was supported by the Russian Foundation for Basic Research (project no. 20-02-00080).

DATA AVAILABILITY

The *GALEX* UV data used in this paper are available in the Barbara A. Miculski Archive for space telescopes at <https://galex.stsci.edu>. The H α data for NGC 895 and NGC 5474, and 8 μ m *IRAC* data for NGC 6946 are available in NASA/IPAC Extragalactic Database at <http://ned.ipac.caltech.edu>. The *UBVRI* data for the galaxies and H α data for NGC 6946 can be shared on reasonable request to the corresponding author.

REFERENCES

- Ashman K. M., Bird C. M., Zepf S. E., 1994, *AJ*, **108**, 2348
- Artamonov B. P. et al., 2010, *Astron. Rep.*, **54**, 1019
- Bastian N., Gieles M., Efremov Yu. N., Lamers H. J. G. L. M., 2005, *A&A*, **443**, 79
- Beck R., Loiseau N., Hummel E., Berkhuijsen E. M., Grave R., Wielebinski, R., 1989, *A&A*, **222**, 58
- Efremov Y. N., 2009, *Astron. Lett.*, **35**, 507
- Efremov Y. N., 2010, *MNRAS*, **405**, 1531
- Efremov Y. N., Elmegreen B. G., 1998, *MNRAS*, **299**, 588
- Elmegreen B. G., 1994, *ApJ*, **433**, 39

⁸ <http://www.mpia.de/THINGS>

⁹ <http://adil.ncsa.uiuc.edu/document/02.TH.01>

Elmegreen B. G., 2009, in Andersen J., Bland-Hawthorn J., Nordström B., eds, *Proc. IAU Symp. 254, The Galaxy Disk in Cosmological Context*. Kluwer, Dordrecht, p. 289

Elmegreen B. G., Elmegreen D. M., 1983, *MNRAS*, **203**, 31

Elmegreen B. G., Elmegreen D. M., 2019, *ApJS*, **245**, id. 14

Elmegreen B. G., Elmegreen D. M., Efremov Y. N., 2018, *ApJ*, **863**, 59

Frick P., Beck R., Shukurov A., Sokoloff D., Ehle M., Kamphuis J., 2000, *MNRAS*, **318**, 925

Ghosh S. Jog C. J., 2016, *MNRAS*, **459**, 4057

Gusev A. S., Efremov Y. N., 2013, *MNRAS*, **434**, 313

Gusev A. S., Shimanovskaya E. V., 2020, *A&A*, **640**, id. L7

Gusev A. S. et al., 2016, *MNRAS*, **457**, 3334

Helfer T. T., Thornley M. D., Regan M. W., Wong T., Sheth K., Vogel S. N., Blitz L., Bock D. C.-J., 2003, *ApJS*, **145**, 259

Horne J. H., Baliunas S. L., 1986, *ApJ*, **302**, 757

Iglesias-Páramo J. et al., 2006, *ApJS*, **164**, 38

Inoue S., Yoshida N., 2018, *MNRAS*, **474**, 3466

Inoue S., Takagi T., Miyazaki A., Cooper E. M., Egusa F., Yajima H., 2021, *MNRAS*, **506**, 84

Inutsuka S., Miyama S. M., 1997, *ApJ*, **480**, 681

Jog C. J., Solomon P. M., 1984a, *ApJ*, **276**, 114

Jog C. J., Solomon P. M., 1984b, *ApJ*, **276**, 127

Kendall S., Clarke C., Kennicutt R. C., 2015, *MNRAS*, **446**, 4155

Kendall S., Kennicutt R. C., Clarke C., 2011, *MNRAS*, **414**, 538

Kennicutt R. C., 1998, *ARA&A*, **36**, 189

Kennicutt R. C., Jr. et al., 2003, *PASP*, **115**, 928

Knapen J. H., Stedman S., Bramich D. M., Folkes S. L., Bradley T. R., 2004, *A&A*, **426**, 1135

Landolt A. U., 1992, *AJ*, **104**, 340

Larsen S. S., Brodie J. P., Elmegreen B. G., Efremov Yu. N., Hodge P. W., Richtler T., 2001, *ApJ*, **556**, 801

Leroy A. K., Walter F., Brinks E., Bigiel F., de Blok W. J. G., Madore B., Thornley M. D., 2008, *AJ*, **136**, 2782

Leroy A. K. et al., 2009, *AJ*, **137**, 4670

Marchuk A. A., 2018, *MNRAS*, **476**, 3591

Mattern M., Kainulainen J., Zhang M., Beuther H., 2018, *A&A*, **616**, id. A78

Meurer G. R. et al., 2006, *ApJS*, **165**, 307

Morrissey P. et al., 2005, *ApJ*, **619**, L7

Pascale R., Bellazzini M., Tosi M., Annibali F., Marinacci F., Nipoti C., 2021, *MNRAS*, **501**, 2091

Press W. H., Rybicki G. B., 1989, *ApJ*, **338**, 277

Proshina I. S., Moiseev A. V., Sil'chenko O. K., 2022, *Astron. Lett.*, *in press*

Rafikov R. R., 2001, *MNRAS*, **323**, 445

Romeo A. B., Falstad N., 2013, *MNRAS*, **433**, 1389

Rownd B. K., Dickey J. M., Helou G., 1994, *AJ*, **108**, 1638

Safronov V. S., 1960, *Ann. Astrophys.*, **23**, 979

Scargle J. D., 1982, *ApJ*, **263**, 835

VanderPlas J. T., 2018, *ApJS*, **236**, 16

Walter F., Brinks E., de Blok W. J. G., Bigiel F., Kennicutt R. C., Jr., Thornley M. D., Leroy A., 2008, *AJ*, **136**, 2563

Wilson C. D. et al., 2012, *MNRAS*, **424**, 3050

APPENDIX A: POSITIONS OF LOCAL MAXIMA OF BRIGHTNESS ALONG SPIRAL ARMS AND SEPARATIONS BETWEEN ADJACENT LOCAL MAXIMA OF BRIGHTNESS

Table A1. Galactocentric distances, longitudinal displacements along spiral arms, and separations for local maxima of brightness and their pairs.

n	r_n (kpc)	s_n (kpc)	l_n (kpc)
NGC 895 – S1			
2	1.42	1.05±0.12	0.96±0.17
3	1.93	2.11±0.12	1.06±0.17
4	2.62	3.55±0.12	1.44±0.17
5	3.06	4.45±0.12	0.90±0.17
6	3.53	5.43±0.12	0.98±0.17
7	4.04	6.49±0.12	1.05±0.17
8	4.98	8.46±0.12	1.97±0.17
9	5.92	10.41±0.12	1.95±0.17
10	6.27	11.13±0.12	0.73±0.17
11	7.11	12.86±0.14	1.73±0.20
12	7.82	14.35±0.12	1.48±0.17
13	8.53	15.81±0.12	1.46±0.17
14	9.20	17.22±0.18	1.41±0.26
15	9.94	18.75±0.12	1.52±0.17
16	10.63	20.18±0.12	1.43±0.17
17	11.15	21.26±0.22	1.08±0.31
18	12.27	23.59±0.12	2.33±0.17
19	12.51	24.09±0.12	0.49±0.18
20	13.00	25.10±0.13	1.02±0.18
21	13.77	26.70±0.27	1.60±0.39
22	15.30	29.88±0.15	3.18±0.21
23	16.05	31.44±0.16	1.56±0.23
NGC 895 – S2			
2	2.65	3.60±0.12	2.52±0.17
3	3.63	5.65±0.12	2.05±0.17
4	4.11	6.65±0.12	1.00±0.17
5	5.13	8.76±0.12	2.11±0.17
6	5.54	9.61±0.12	0.85±0.17
7	5.92	10.40±0.12	0.80±0.17
8	6.33	11.26±0.12	0.85±0.17
9	7.04	12.72±0.14	1.46±0.20
10	8.05	14.82±0.12	2.10±0.17
11	8.77	16.33±0.12	1.51±0.17
12	9.75	18.36±0.19	2.03±0.27
13	10.43	19.76±0.21	1.41±0.29
14	11.59	22.17±0.23	2.41±0.33
15	12.27	23.59±0.12	1.42±0.17
16	13.77	26.70±0.27	3.11±0.39
17	14.17	27.53±0.28	0.83±0.40
18	15.89	31.12±0.16	3.59±0.22
NGC 5474 – S1			
2	0.55	0.62±0.02	0.50±0.03
3	0.79	1.04±0.02	0.41±0.03
4	1.02	1.42±0.02	0.39±0.03
5	1.52	2.29±0.02	0.86±0.03
NGC 5474 – S2			
2	1.66	1.09±0.03	0.27±0.04
3	1.82	1.69±0.02	0.60±0.03
4	2.12	2.83±0.04	1.14±0.05
5	2.29	3.47±0.02	0.64±0.03
6	2.47	4.16±0.02	0.69±0.03
7	2.66	4.85±0.02	0.69±0.03
8	2.78	5.35±0.02	0.49±0.04
9	2.89	5.76±0.03	0.41±0.04
10	3.41	7.69±0.06	1.93±0.09
11	3.61	8.45±0.03	0.76±0.05
12	3.95	9.75±0.04	1.30±0.05
13	4.16	10.56±0.04	0.81±0.05

Table A1. Continued

n	r_n (kpc)	s_n (kpc)	l_n (kpc)
NGC 5474 – S3			
2	2.23	0.96±0.04	0.79±0.06
3	2.51	1.68±0.05	0.72±0.07
4	2.83	2.54±0.03	0.86±0.04
5	2.98	2.92±0.06	0.38±0.08
6	3.27	3.69±0.03	0.77±0.04
7	3.42	4.07±0.03	0.38±0.04
8	3.68	4.74±0.03	0.67±0.05
9	3.81	5.09±0.04	0.35±0.05
10	3.98	5.53±0.04	0.44±0.05
11	4.50	6.89±0.04	1.36±0.06
12	4.88	7.87±0.05	0.97±0.06
13	5.13	8.53±0.05	0.66±0.07
NGC 6946 – S1			
2	1.09	0.34±0.02	0.11±0.02
3	1.15	0.46±0.02	0.11±0.02
4	1.27	0.70±0.03	0.24±0.04
5	1.59	1.33±0.02	0.63±0.02
6	1.69	1.53±0.02	0.20±0.02
7	1.85	1.85±0.02	0.32±0.03
8	2.04	2.24±0.02	0.39±0.03
9	2.22	2.59±0.02	0.34±0.03
10	2.43	3.01±0.02	0.42±0.03
11	2.69	3.53±0.03	0.52±0.04
12	2.89	3.92±0.03	0.39±0.04
13	3.10	4.35±0.03	0.42±0.04
14	3.30	4.73±0.03	0.39±0.05
15	3.51	5.15±0.07	0.41±0.10
16	3.62	5.36±0.04	0.22±0.05
17	4.13	6.38±0.04	1.02±0.06
18	4.30	6.72±0.04	0.34±0.06
19	4.43	6.98±0.05	0.26±0.06
20	4.61	7.35±0.05	0.37±0.07
21	4.86	7.83±0.05	0.48±0.07
22	5.06	8.23±0.05	0.40±0.07
23	5.27	8.64±0.05	0.42±0.08
24	5.60	9.30±0.06	0.66±0.08
25	5.77	9.64±0.06	0.34±0.08
NGC 6946 – S1 (IR)			
2	1.69	1.53±0.03	1.23±0.05
3	1.83	1.81±0.03	0.28±0.05
4	2.22	2.59±0.03	0.77±0.05
5	2.53	3.21±0.03	0.62±0.05
6	2.86	3.86±0.03	0.65±0.05
7	3.13	4.41±0.03	0.55±0.05
8	3.30	4.73±0.03	0.32±0.05
9	3.44	5.01±0.03	0.27±0.05
10	3.62	5.36±0.04	0.36±0.05
11	3.80	5.74±0.04	0.38±0.05
12	4.04	6.21±0.04	0.47±0.06
13	4.25	6.63±0.04	0.42±0.06
14	4.86	7.82±0.05	1.19±0.07
15	5.43	8.97±0.05	1.14±0.08
16	5.54	9.19±0.06	0.22±0.08
17	5.89	9.88±0.06	0.69±0.08
NGC 6946 – S2			
2	1.27	0.70±0.02	0.27±0.02
3	1.48	1.11±0.02	0.41±0.02
4	1.74	1.63±0.02	0.52±0.03
5	2.09	2.33±0.02	0.69±0.03
6	2.41	2.96±0.02	0.63±0.03

Table A1. Continued

n	r_n (kpc)	s_n (kpc)	l_n (kpc)
NGC 6946 – S2			
7	2.58	3.31±0.03	0.35±0.04
8	2.92	3.98±0.03	0.67±0.04
9	3.13	4.41±0.03	0.43±0.04
10	3.30	4.73±0.03	0.32±0.05
11	3.51	5.15±0.07	0.41±0.10
12	3.73	5.58±0.04	0.44±0.05
13	3.88	5.89±0.04	0.31±0.06
14	4.04	6.21±0.04	0.32±0.06
15	4.25	6.63±0.04	0.42±0.06
16	4.43	6.98±0.09	0.35±0.13
17	4.95	8.02±0.05	1.04±0.07
18	5.11	8.33±0.05	0.30±0.07
19	5.32	8.75±0.05	0.42±0.08
20	5.66	9.41±0.06	0.66±0.08
21	5.89	9.88±0.06	0.47±0.08
NGC 6946 – S2 (IR)			
2	1.24	0.65±0.03	0.35±0.05
3	1.69	1.53±0.03	0.88±0.05
4	1.98	2.12±0.03	0.59±0.05
5	2.13	2.41±0.03	0.29±0.05
6	2.58	3.31±0.03	0.90±0.05
7	2.72	3.58±0.03	0.27±0.05
8	2.98	4.10±0.03	0.52±0.05
9	3.30	4.73±0.03	0.63±0.05
10	3.61	5.36±0.04	0.63±0.05
11	4.08	6.29±0.04	0.93±0.06
12	4.25	6.63±0.04	0.34±0.06
13	4.48	7.07±0.04	0.44±0.06
14	4.90	7.92±0.05	0.85±0.07
15	5.16	8.43±0.05	0.51±0.07
16	5.60	9.30±0.06	0.87±0.08
NGC 6946 – S3			
2	1.78	0.65±0.02	0.34±0.03
3	1.91	0.92±0.02	0.26±0.03
4	2.04	1.16±0.02	0.24±0.03
5	2.13	1.33±0.02	0.17±0.03
6	2.34	1.74±0.02	0.41±0.03
7	2.49	2.03±0.02	0.29±0.04
8	2.65	2.35±0.03	0.31±0.04
9	2.94	2.91±0.03	0.57±0.04
10	3.24	3.48±0.03	0.57±0.04
11	3.63	4.25±0.04	0.77±0.05
12	3.83	4.63±0.08	0.38±0.11
13	4.03	5.03±0.04	0.40±0.06
14	4.38	5.71±0.04	0.68±0.06
15	4.62	6.17±0.05	0.46±0.07
16	4.82	6.56±0.05	0.38±0.07
17	4.97	6.85±0.05	0.30±0.07
18	5.24	7.37±0.05	0.52±0.07
19	5.58	8.04±0.06	0.66±0.08
NGC 6946 – S3 (IR)			
2	1.74	0.58±0.03	0.43±0.05
3	1.96	1.00±0.03	0.41±0.05
4	2.19	1.46±0.03	0.46±0.05
5	2.39	1.83±0.03	0.37±0.05
6	2.65	2.35±0.03	0.51±0.05
7	2.91	2.85±0.03	0.51±0.05
8	3.17	3.35±0.03	0.50±0.05
9	3.45	3.89±0.03	0.54±0.05
10	3.79	4.55±0.04	0.66±0.05

Table A1. Continued

n	r_n (kpc)	s_n (kpc)	l_n (kpc)
NGC 6946 – S3 (IR)			
11	3.99	4.95 ± 0.04	0.40 ± 0.06
12	4.25	5.45 ± 0.04	0.50 ± 0.06
13	4.43	5.80 ± 0.04	0.35 ± 0.06
14	4.92	6.75 ± 0.05	0.95 ± 0.07
15	5.35	7.59 ± 0.05	0.84 ± 0.08
16	5.52	7.92 ± 0.06	0.33 ± 0.08
17	5.82	8.50 ± 0.06	0.58 ± 0.08
NGC 6946 – S4			
2	1.86	0.80 ± 0.02	0.59 ± 0.03
3	2.06	1.20 ± 0.02	0.40 ± 0.03
4	2.41	1.88 ± 0.02	0.68 ± 0.03
5	2.60	2.24 ± 0.03	0.36 ± 0.04
6	2.88	2.80 ± 0.03	0.56 ± 0.04
7	3.20	3.41 ± 0.03	0.62 ± 0.05
8	3.52	4.03 ± 0.07	0.62 ± 0.10
9	3.87	4.71 ± 0.04	0.68 ± 0.06
10	4.03	5.03 ± 0.04	0.32 ± 0.06
11	4.25	5.45 ± 0.04	0.42 ± 0.06
12	4.43	5.80 ± 0.09	0.35 ± 0.13
13	4.87	6.65 ± 0.05	0.85 ± 0.07
14	5.08	7.06 ± 0.05	0.41 ± 0.07
15	5.47	7.81 ± 0.06	0.75 ± 0.08
16	5.64	8.15 ± 0.06	0.34 ± 0.08
17	6.01	8.86 ± 0.06	0.71 ± 0.09
18	6.46	9.75 ± 0.07	0.89 ± 0.09
19	6.88	10.56 ± 0.07	0.81 ± 0.10
NGC 6946 – S4 (IR)			
2	1.71	0.51 ± 0.03	0.39 ± 0.05
3	1.88	0.84 ± 0.03	0.33 ± 0.05
4	2.06	1.20 ± 0.03	0.36 ± 0.05
5	2.46	1.98 ± 0.03	0.78 ± 0.05
6	2.97	2.97 ± 0.03	0.99 ± 0.05
7	3.27	3.55 ± 0.03	0.57 ± 0.05
8	3.48	3.96 ± 0.03	0.41 ± 0.05
9	4.16	5.28 ± 0.04	1.32 ± 0.06
10	4.38	5.71 ± 0.04	0.43 ± 0.06
11	4.82	6.56 ± 0.05	0.84 ± 0.07
12	5.03	6.96 ± 0.05	0.40 ± 0.07
13	5.47	7.81 ± 0.06	0.85 ± 0.08
14	5.82	8.50 ± 0.06	0.69 ± 0.08
15	6.67	10.15 ± 0.07	1.65 ± 0.10
16	6.88	10.56 ± 0.07	0.41 ± 0.10